Granular Matter (2016) 18:21
DOI 10.1007/s10035-016-0626-0

ORIGINAL PAPER

A coupled discrete element-finite difference model of selective laser sintering

Rishi Ganeriwala[1,2] · **Tarek I. Zohdi**[3]

Received: 12 August 2015

Abstract Selective laser sintering (SLS) is an additive manufacturing technology whereby one can 3D print parts out of a powdered material. However, in order to produce defect free parts of sufficient strength, the process parameters (laser power, scan speed, powder layer thickness, etc.) must be carefully optimized depending on material, part geometry, and desired final part characteristics. Computational methods are very useful in the quick optimization of such parameters without the need to run numerous costly experiments. Most published models of this process involve continuum-based techniques, which require the homogenization of the powder bed and thus do not capture the stochastic nature of this process. Thus, the aim of this research is to produce a reduced order computational model of the SLS process which combines the essential physics with fast computation times. In this work the authors propose a coupled discrete element-finite difference model of this process. The powder particles are modeled as discrete, thermally and mechanically interacting spheres. The solid, underneath substrate is modeled via the finite difference method. The model is validated against experimental results in the literature and three-dimensional simulations are presented.

✉ Rishi Ganeriwala
rkganeri@berkeley.edu

[1] Department of Mechanical Engineering, 6102 Etcheverry Hall, University of California, Berkeley, CA 94720-1740, USA

[2] Present Address: Lawrence Livermore National Laboratory, Livermore, CA 94550, USA

[3] Department of Mechanical Engineering, 6117 Etcheverry Hall, University of California, Berkeley, CA 94720-1740, USA

Keywords Additive manufacturing · Selective laser sintering · Selective laser melting · Computational mechanics · Discrete elements

1 Introduction

Selective laser sintering (SLS) is an additive manufacturing (AM) technique whereby one can effectively 3D print parts out of a powdered material directly from a CAD file. It is often used in rapid prototyping, tooling, and manufacturing (RP, RT, and RM). The original SLS process was invented in 1986 at the University of Texas at Austin [35], with applications that are quickly increasing as the technology matures. Note that selective laser melting (SLM) is an identical process to SLS, with the difference being that full melting occurs in SLM, used for the production of fully dense metal parts.

Figure 1 depicts a schematic of a typical SLS machine. In this process, first a thin layer of powder particles, with sizes ranging from approximately 10–100 μm, is deposited onto a substrate via a roller or wiper blade. Each layer is typically on the order of 20–100 μm thick. Many different powder materials can be used including metals, polymers, ceramics, and composites. A laser is then directed via a scanner system over the powders in the pattern of the desired shape, either partially melting (SLS) or fully melting (SLM) the powders. As the laser selectively melts the particles, they fuse and bond together. Next, the fabrication bed lowers, a new layer of powder is placed on top by the roller, and the laser selectively scans over the surface again. This layer-by-layer, AM process is repeated until the final part has been fabricated.

The laser beam generally has a nominal diameter on the order of 0.5 mm or less. A pulsed or continuous wave CO_2 laser is typically used for polymer materials, while an Nd:YAG or fiber laser is used for metals. The reason

Published online: 26 March 2016

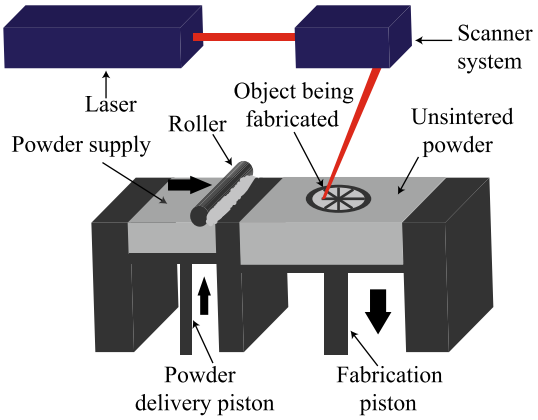

Fig. 1 Schematic of a typical SLS/SLM set-up

for this lies in the fact that polymers and ceramics (oxides) absorb the 10.6 μm wavelength emitted by the CO_2 laser better, while metals and ceramics (carbides) better absorb the 1.06 or 1.08 μm wavelengths emitted by Nd:YAG or fiber lasers, respectively [22]. The laser power can vary anywhere from approximately 30–400 W depending on the material and desired part characteristics. Scan speed may be varied from 2 to 700 cm/s or more. In SLS, a binder material with a lower melting temperature may be applied to the particles. This binder material is melted, bonding together particles with higher melting temperatures. To aid in the process, the sintering chamber is often heated to minimize required laser energy and expedite the process. Preheating the chamber has the added benefit of reducing thermal gradients and thus reducing the residual stresses present in the final part. Additionally, an inert gas, usually nitrogen or argon, is present to avoid oxidation or burning of the powders.

Upon completion of the process, the final part is removed and often bead blasted to remove unsintered, adhering particles [35]. In the case of SLS, the final parts may still have a significant amount of porosity. In such cases, additional operations (i.e. hot isostatic pressing or infiltration) are also required to increase the part density, depending on the application [21]. Due to the high heating and cooling rates present in SLM (up to 10^6 °C/s) large residual stresses may build up in the final part. This high cooling rate also causes anisotropy of the final part as long thin grains form, oriented along the vertical build direction. This inhibits the formation of certain microstructures (typically martensitic microstructures are formed) [22]. Post SLS/SLM heat treating can be performed to relieve residual stresses and change the microstructure.

Laser sintering or melting has the advantage of being able to rapidly produce parts of relatively complex geometries, in a timely and cost effective manner. It is especially useful in its ability to make metallic parts, which would otherwise be impossible to form using other RP, RT, and RM techniques as shown in the works by Simchi [33] and Simchi and Pohl [34]. Fischer et al. [9] and Maeda and Childs [25] have demonstrated the ability for SLM to produce parts made from hard metal powders, such as WC–Co and TiC–Ni used in machining tools and abrasion resistant coatings. SLS has also seen uses in RP and RM for polymeric and ceramic materials. Schmidt et al. [31], Tan et al. [36], and Williams et al. [38] have successfully laser sintered polymeric biomaterials which can be used to produce tissue engineering scaffolds and certain types of implants. SLS/SLM is also currently employed to produce parts in the automotive, aerospace, medical, and energy industries, among others.

While there are clearly a vast, and growing, number of applications for this process, if not performed correctly the resulting parts can have many defects, especially high residual stresses, microcracking, warping, delamination of layers, and/or high porosity. An optimal set of process parameters needs to be applied to ensure high quality of the finished product. Such process parameters may include (but certainly are not limited to) laser power, scan speed, spot size, and hatch spacing (distance between successive parallel passes of the laser). Additionally the powder material, powder size distribution, layer thickness, loose powder density, laser scan strategy, surrounding atmosphere, and preheat temperature can significantly affect final part quality. Clearly, the optimal set of parameters will vary depending on material and desired final part characteristics. Thus a computational model of the process which can capture all these process parameters would be of great value to operators of SLS/SLM equipment and would lessen the need for costly, and time-consuming experiments.

Many researchers have already proposed different ways to simulate this process (see Zeng et al. [39] for a very detailed review of many different approaches). Dong et al. [7] and Kolossov et al. [18] have created 3D finite element (FE) models for the temperature evolution during laser sintering. The latter model also predicts densification. Matsumoto et al. [26] proposed a FE method for calculating the temperature and stress distribution in a single layer of sintered material. Hodge et al. [15] used a 3D coupled thermal-mechanical FE model to look at part-scale simulations and investigate optimal conditions for the fabrication of overhanging sections. Antony et al. [3] used FE and experimental analysis to look at SLM of 316L stainless steel powders. Investigation was made into the effects of wetting angle and balling, where the melt pool will tend to ball up rather than forming one continuous track (often attributed to Raleigh instabilities) if the length to width ratio of the track is too high. Nelson et al. [29] used empirical data to create a 1D heat transfer model of SLS that can predict sintering depths. Simchi [33] and Simchi and Pohl [34] used empirical results to determine a relationship between energy input and densification during SLS.

Korner et al. [19] used a modified Lattice Boltzmann approach to produce a 2D model of selective electron beam melting (SEBM) and followed up on this by successively assembling multiple layers using the same approach in a later work [20]. This work captures the stochastic nature of the powder bed and showed that loose powder bed density had the biggest effect on final part density. Dai and Gu [6] used a commercial Finite Volume software to simulate SLM for copper alloys. Effects such as Marangoni (surface tension driven) convection and entrapped gas bubbles are included in this simulation, which is compared with experiments in predicting resultant part density. Gusarov and Kruth [12] provide an analytical equation for the penetration of a laser into a powder bed as a function of powder bed density and particle size. This work was followed with a Finite Difference (FD) simulation of heat transfer during SLM [13]. Khairallah and Anderson [17] use a multiphysics Arbitrary Lagrangian Eulerian (ALE) code to fully simulate the SLM process. This approach appears novel in that individual particles are modeled and meshed up in determining the melt pool size. Additionally, the effect of surface tension on melt pool geometry is demonstrated. However, this approach requires an extremely large computational effort to simulate relatively short time and length scales.

In many of the previously described works, the material was treated as a continuum medium and effective material properties were used. Additionally, due to the difficulty of accounting for localized phase change in FE models, this effect was often neglected. Empirical models have the drawback of often being process and material specific. Other models are extremely computationally expensive.

In this work, a reduced order, discrete element (DE) model is proposed to simulate the deposition and subsequent laser sintering of the powdered particles. The interaction of a single layer of these DE particles with an underneath substrate is also modeled. The solid substrate is modeled via the FD method. Note that previously solidifed underneath layers could also be modeled using this technique. The DE–FD thermal coupling mechanism is described and, to the authors' knowledge, is novel, especially with regards to SLS modeling. An algorithm for dealing with the change in material properties due to phase changes is presented. This approach has the advantage of eliminating the need of using homogenized effective properties for the powder bed, can capture particle dynamics and the stochastic nature of the powder bed, and yet is computationally cheap enough such that the simulation time is on the order of minutes to hours on a single laptop computer. This allows for quick optimization of process parameters for different materials and/or powder size distributions. Validation is offered through comparison against experimental results in the literature. Additional 3D simulation results and parameter studies are discussed. Finally, conclusions are drawn, along with future work to be done on this topic.

2 Modeling approach

A multiphysical modeling approach has been employed to simulate the SLS process for a single layer of particles. A discrete element approach was used to model particle-to-particle and particle-to-wall mechanical and thermal interactions. Particle to underneath substrate interactions are modeled using the finite difference method for the solid substrate. Each particle is idealized as a sphere and the temperature of each sphere is assumed to be uniform throughout that individual particle, due to the low Biot numbers and in an effort to reduce computation time. Additionally, we assume that the particles are small enough so that the effect of their rotations with respect to their center of mass is negligible to their overall motion. That is to say, rotation of individual particles due to external torques is not modeled. The modeling approach can be characterized in two parts: (1) simulation of the deposition of the powder particles; (2) simulation of the temperature evolution of the particles and underneath substrate after a single pass of a laser beam. The computational domain in this simulation is a box with cross section of 1 mm $\times$ 0.5 mm. The model builds upon a previous work by the authors [11] and follows approaches previously developed in other works by Campello and Zohdi [5] and Zohdi [40–42].

2.1 Particle dynamics

A simple model of the deposition of the particles is described in this section. In an effort to simplify the layer deposition process, the authors assume that the particles are being dropped into the domain from a small height of 0.3 mm or less. These particles are allowed to settle themselves into a layer by gravity. Note that this is not a completely accurate simulation of the powder deposition process in SLS, as typically a roller or wiper blade is used. However, since the powder layer is typically not mechanically compressed during deposition, the authors believe this approach is sufficient to approximate the formation of a single layer of powder particles.

Starting from Newton's second law, we can determine an equation for the motion of the i-th particle (starting from a sample of N non-intersecting particles):

$$m_i \ddot{\mathbf{x}}_i = \mathbf{F}_i^{total} = \mathbf{F}_i^{con} + \mathbf{F}_i^{fric} + \mathbf{F}_i^{env} + \mathbf{F}_i^{grav}, \tag{1}$$

where m represents mass, $\mathbf{x}$ represents position, $\mathbf{F}^{con}$ is the contact force, $\mathbf{F}^{fric}$ is the force due to friction, $\mathbf{F}^{env}$ represents environmental forces, and $\mathbf{F}^{grav}$ is the force due to gravity.

The contact force, $\mathbf{F}_i^{con}$, is modeled via a standard Hertzian contact model for intersecting spheres [16]. This theory assumes that the contact area between the particles is small with respect to the dimensions of each particle and with respect to the relative radii of curvature of the surfaces. Additionally, the strains are considered small and within the elastic limit, and the surfaces are considered frictionless. These assumptions can certainly be justified for the case of elastically loaded, smooth metallic spheres, as is the case in the present work. It should be noted here that although Hertzian contact theory assumes a frictionless surface in its derivation, this does not mean that friction must be neglected entirely, for reasons that shall be discussed later in this section.

If the distance between two particles (i and j) is less than the combined radii of the particles, then a particle-to-particle normal contact force exists:

If $\|\mathbf{x}_j - \mathbf{x}_i\| \leq (R_i + R_j)$, then

$$\mathbf{F}_{ij}^{con} = -\frac{4}{3}\sqrt{R^*}E^*\delta_{ij}^{3/2}\mathbf{n}_{ij} + d\dot{\delta}_{ij}\mathbf{n}_{ij}, \tag{2}$$

$$\mathbf{F}_i^{con} = \sum_{j=1}^{N_c}\mathbf{F}_{ij}^{con}, \tag{3}$$

where N_c is the number of particles in contact with particle i, R^* and E^* are the effective radius and Young's modulus of the interacting particles given by

$$R^* = \frac{R_i R_j}{R_i + R_j}, \tag{4}$$

$$E^* = \frac{E_i E_j}{E_j(1-\nu_i^2) + E_i(1-\nu_j^2)}. \tag{5}$$

Here R_i, E_i, and ν_i represent the radius, Young's modulus, and Poisson's ratio, respectively, of particle i. In Eq. 2, δ_{ij} is defined as a positive number indicating the overlap between particles i and j (see Fig. 2)

$$\delta_{ij} = \left|\|\mathbf{x}_j - \mathbf{x}_i\| - (R_i + R_j)\right|. \tag{6}$$

The rate of change of overlap $\dot{\delta}_{ij}$ is given by

$$\dot{\delta}_{ij} = (\mathbf{v}_j - \mathbf{v}_i)\cdot\mathbf{n}_{ij}, \tag{7}$$

where $\mathbf{v}$ represents velocity and $\mathbf{n}_{ij}$ is the unit normal vector between particles i and j, calculated as

$$\mathbf{n}_{ij} = \frac{\mathbf{x}_j - \mathbf{x}_i}{\|\mathbf{x}_j - \mathbf{x}_i\|}. \tag{8}$$

Finally the damping parameter d in Eq. 2 is calculated according to the method of Wellmann and Wriggers [37], where

$$d = 2\zeta\sqrt{2E^* m^* \sqrt{R^*}\delta_{ij}^{1/4}}. \tag{9}$$

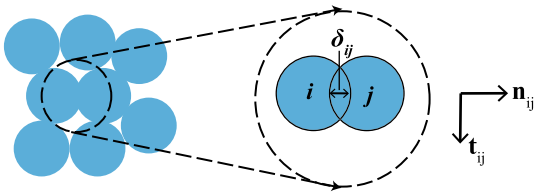

Fig. 2 Particle-to-particle overlap

In Eq. 9, $m^* = \frac{m_i m_j}{m_i + m_j}$, is the effective mass and ζ is a damping parameter that must be set. $\zeta = 1$ is critically damped, $\zeta > 1$ is overdamped, and $\zeta < 1$ is less than critically damped. Note that if $\zeta = 0$, there is no damping force, as in an elastic collision.

In the case of particle contact with a wall, the same contact model is used except that we now replace the property values of particle j with those of the wall. In the case of the effective radius, we take the limit as $R_j \to \infty$, which yields $R^* = R_i$. The overlap is given by

$$\delta_{iw} = |\|\mathbf{x}_w - \mathbf{x}_i\| - R_i|, \tag{10}$$

where $\mathbf{x}_w$ refers to the point on the wall closest to the particle's center of mass. The rate of change of overlap is

$$\dot{\delta}_{iw} = -\mathbf{v}_i\cdot\mathbf{n}_{iw}, \tag{11}$$

assuming the walls are stationary. The normal vector $\mathbf{n}_{iw}$ is the unit vector orthogonal to the plane of the wall, facing in the direction of the particle.

As mentioned earlier, Hertzian contact theory assumes a frictionless surface when calculating the normal forces. However, recognizing that friction forces act in a tangential direction, they do not significantly affect the normal forces calculated via Hertzian theory for contacting spheres in the absence of additional tangential loading [2]. This allows for the addition of tangential friction forces to the normal forces obtained from Hertzian contact mechanics. To model friction forces between particle-to-particle or particle-to-wall collisions, we assume a continuous sliding model for simplicity. The friction force is given by

$$\mathbf{F}_{ij}^{fric} = \mu_d \parallel \mathbf{F}_{ij}^{con} \parallel \mathbf{t}_{ij}, \tag{12}$$

$$\mathbf{F}_i^{fric} = \sum_{j=1}^{N_c}\mathbf{F}_{ij}^{fric}. \tag{13}$$

In Eq. 12, μ_d is the dynamic coefficient of friction and $\mathbf{t}_{ij}$ is the unit tangential vector between the particles, given by

$$\mathbf{t}_{ij} = \frac{\mathbf{v}_{tj} - \mathbf{v}_{ti}}{\parallel \mathbf{v}_{tj} - \mathbf{v}_{ti} \parallel}, \tag{14}$$

where $\mathbf{v}_t$ represents the tangential velocity, $\mathbf{v}_{ti} = \mathbf{v}_i - (\mathbf{v}_i \cdot \mathbf{n}_{ij})\mathbf{n}_{ij}$. Again the frictional force between the particles and the wall is modeled in the same manner as for two particles except that the velocity of the wall (equal to $\mathbf{0}$ in this simulation) replaces the velocity of particle j.

Note that a stick-slip friction model could be introduced without too much additional effort, but it was deemed unimportant to the overall simulation as we are more concerned with thermal effects during laser heating and the particles no longer move after they have settled into equilibrium (although investigation is currently ongoing into the effects of radiative pressure on the powder bed as the laser passes over the powder particles).

The environmental force, $\mathbf{F}_i^{env}$, comes into play as a force opposing the motion of the particle due to the surrounding environment (i.e. drag force as the particle moves through the ambient environment). This environmental force could also be used to model the effects of lubricant binders which may be placed in the powdered material. Assuming that no binders are present, we approximate this environmental force with Stoke's drag [28]:

$$\mathbf{F}_i^{env} = -6\pi\mu_f R_i \mathbf{v}_i, \tag{15}$$

where μ_f is the dynamic viscosity of the fluid in the sintering chamber (argon in this simulation). Note that Stoke's flow is a valid approximation only in situations where the Reynold's number is well below unity, i.e. $Re \ll 1$. This condition is satisfied in the present situation since the radius of the particles and the velocities experienced are both small.

Finally there exists the gravitational force, $\mathbf{F}_i^{grav}$, which is the driving force causing the particles to settle in a layer. The gravitational force acts in a downwards, or $-\mathbf{z}$, direction and is given by

$$\mathbf{F}_i^{grav} = -m_i g\hat{\mathbf{z}}, \tag{16}$$

where $\hat{\mathbf{z}}$ is the unit vector in the $\mathbf{z}$ direction.

2.2 Particle thermal effects

Assuming a lumped capacitance model where the temperature field is uniform throughout each particle (consistent with the low Biot numbers resulting from the small particle sizes), the thermal governing equation in integral form is

$$\int_{\partial\omega} \mathbf{Q}\cdot\mathbf{n}dA + \int_{\omega} HdV = \int_{\omega} \rho c\dot{T}dV, \tag{17}$$

where $\mathbf{Q}$ represents heat transfer, H is a source term to account for laser heat input, ρ is density, c is the constant pressure specific heat capacity of the material, T is temperature, and ω represents the domain of interest. Discretizing

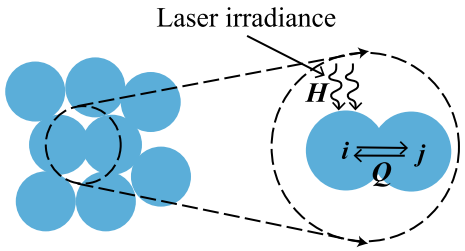

Fig. 3 Heat transfer to an individual particle

Eq. 17 over each particle (see Fig. 3) we obtain

$$Q_i + H_i = m_i c_i \dot{T}_i. \tag{18}$$

We then break down the heat transfer term in Eq. 18 into it's conductive, convective, and radiative parts. Neglecting particle-to-gas conduction in the gaps between particles due to the much lower thermal conductivity of the gas environment, we get

$$\begin{aligned} Q_i &= Q_i^{cond} + Q_i^{conv} + Q_i^{rad} \\ &= \sum_{j=1}^{N_c} K\frac{T_j - T_i}{\|\mathbf{x}_j - \mathbf{x}_i\|}A_{ij} + h_{conv}(T_i - T_{env})A_i \\ &\quad + \epsilon\sigma_{SB}(T_i^4 - T_{env}^4)A_i. \end{aligned} \tag{19}$$

In Eq. 19 K is the thermal conductivity of the material (assuming it is isotropic), A_{ij} is the contact area between particles i and j, h_{conv} is the convective heat transfer coefficient, ϵ is the material emissivity, σ_{SB} is the Stefan–Boltzmann constant ($\sigma_{SB} = 5.67 \times 10^{-8}\mathrm{W/m^2\,K^4}$), and $A_i = \pi R_i^2$ is the projection of the particle's surface area facing the surrounding environment. Note that convective and radiative heat transfer is assumed to only occur for exposed particles on the top surface. Thus these particles will exchange heat with the environment, which is at a temperature of T_{env}. Convective and radiative heat transfer is not considered for particles not on the top, exposed layer. For two contacting particles the contact area (see Fig. 4) is given by

$$A_{ij} = \pi h^2 = \pi\left(R_i \sin\left(\arccos\left(\frac{R_j^2 - R_i^2 - d^2}{-2dR_i}\right)\right)\right)^2, \tag{20}$$

where $d = \|\mathbf{x}_j - \mathbf{x}_i\|$. The law of cosines is invoked in the derivation of the previous equation.

Assuming a Gaussian laser is used, the laser heating term, H_i in Eq. 18, is given as

$$H_i = \alpha I(r,z)A_i, \tag{21}$$

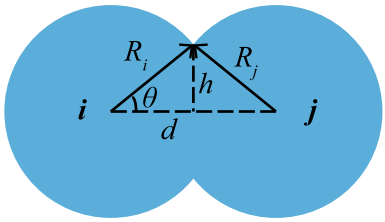

Fig. 4 Contact area of two intersecting particles

where α is the absorptivity of the material at the wavelength of the laser ($0 \leq \alpha \leq 1$), $I(r, z)$ is the laser intensity (W/m^2) as a function of radial distance (r) and depth (z) from the beam center, and $A_i = \pi R_i^2$ is the projected area of the particle receiving direct, normal radiation from the laser.

The laser beam is assumed to be Gaussian (as is often the case in the SLS process) so that the intensity decreases exponentially as radial distance from the beam's center increases. A Beer-Lambert type model for the laser penetration is used, where the intensity is assumed to decrease exponentially as a function of penetration depth. Thus the intensity can be expressed as

$$I(r, z) = I_0 e^{-\beta z} e^{(-2r^2/w^2)}, \tag{22}$$

where $I_0 = \frac{2 \times Power}{\pi w^2}$ is the peak intensity, w is the beam spot size measured to where the intensity falls to $1/e^2$ of the peak intensity, and β is the optical extinction coefficient [14]. Note that the laser energy will penetrate much deeper in a powder bed than a solid material due to the multiple reflections that take place off the powder particles. The optical extinction coefficient for a metal powder bed is modeled according to the theory of Gusarov et al. [12,13]. In this theory the extinction coefficient for a homogeneous absorbing powder is given as a function of the powder bed porosity, γ, and the particle diameter, D. Penetration of the laser to the underlying substrate is also taken into account during this derivation. This model has been shown to agree with ray tracing simulations in the limit of a deep powder bed [12] and is given as

$$\beta = \frac{3(1-\gamma)}{2\gamma D}. \tag{23}$$

To account for phase change as the material heats up and subsequently melts, the apparent heat capacity method is used, similar to the method outlined by Bonocina et al. [4] and more recently by Muhieddine et al. [27]. In this technique, the energy needed for phase change to happen is taken into account by computationally raising the specific heat of the material in a small range (ΔT) around the melting or vaporization temperature. The algorithm is outlined as follows and can be graphically seen in Fig. 5:

$$c = \begin{cases} c_{solid}, & T < T_m - \frac{\Delta T}{2} \\ \frac{c_{solid} + c_{liquid}}{2} + \frac{L_{m/s}}{\Delta T}, & T_m - \frac{\Delta T}{2} \leq T \leq T_m + \frac{\Delta T}{2} \\ c_{liquid}, & T_m + \frac{\Delta T}{2} < T < T_v - \frac{\Delta T}{2} \\ \frac{c_{liquid} + c_{gas}}{2} + \frac{L_{v/c}}{\Delta T}, & T_v - \frac{\Delta T}{2} \leq T \leq T_v + \frac{\Delta T}{2} \\ c_{gas}, & T > T_v + \frac{\Delta T}{2} \end{cases} \tag{24}$$

where T_m is the melting temperature, T_v is the vaporization (or boiling) temperature, $L_{m/s}$ is the latent heat of melting or solidification, and $L_{v/c}$ is the latent heat of vaporization or condensation.

2.3 Finite difference modeling of substrate

The finite difference method is employed to model heating of the solid substrate underneath the powder particles. The substrate is considered to be a rectangular box with dimensions $L_x \times L_y \times L_z$. To represent conduction within the substrate we can recast Eq. 17 as

$$\begin{aligned} \rho c \dot{T} &= \nabla \cdot (K \nabla T) + H \\ &= \frac{\partial}{\partial x}\left(K \frac{\partial T}{\partial x}\right) + \frac{\partial}{\partial y}\left(K \frac{\partial T}{\partial y}\right) + \frac{\partial}{\partial z}\left(K \frac{\partial T}{\partial z}\right) + H. \end{aligned} \tag{25}$$

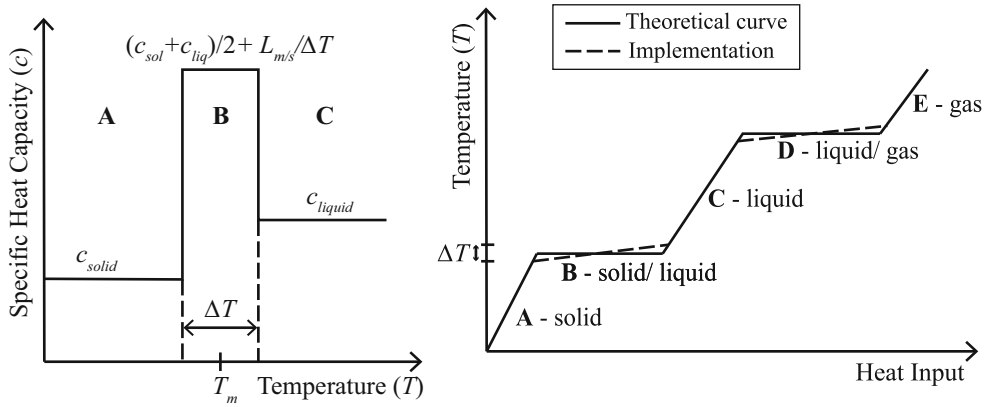

Fig. 5 Illustration of how heat capacity is updated (*left*) and ensuing phase change diagram (*right*)

Using a second order accurate, centered difference approximation for the partial derivatives in space we obtain

$$\frac{\partial}{\partial x}\left(K\frac{\partial T}{\partial x}\right) \approx \frac{1}{\Delta x}\left(\frac{K(x+\Delta x,y,z)+K(x,y,z)}{2}\right) \times \left(\frac{T(x+\Delta x,y,z)-T(x,y,z)}{\Delta x}\right) - \frac{1}{\Delta x}\left(\frac{K(x,y,z)+K(x-\Delta x,y,z)}{2}\right) \times \left(\frac{T(x,y,z)-T(x-\Delta x,y,z)}{\Delta x}\right). \tag{26}$$

We can discretize $\frac{\partial}{\partial y}\left(K\frac{\partial T}{\partial y}\right)$ and $\frac{\partial}{\partial z}\left(K\frac{\partial T}{\partial z}\right)$ in an analogous manner.

To solve Eq. 25 using the FD scheme, it is necessary to prescribe appropriate boundary conditions (BCs) on the faces of the domain. Since the domain is much larger than the spot size of the laser beam, fixed Dirichlet boundary conditions (i.e. $T(0,y,z) = T(L_x,y,z) = T(x,0,z) = T(x,L_y,z) = T(x,y,0) = T_0$) were prescribed on all side faces and the bottom face of the substrate mesh, as shown in Fig. 6. T_0 is the preheat temperature of the powder bed. A Neumann, flux-type BC was prescribed on the top face by calculating conductive heat transfer from the discrete element particles to the substrate. This heat transfer amount (in units of W) was divided by the area of one grid square on the top layer of the FD mesh to calculate the flux (W/m^2) experienced by those mesh points. Each nodal point is assumed to receive 1/4 of the total heat flux experienced by the square enclosed by those points (see Fig. 6). Any laser irradiation which managed to penetrate through the powder layer and onto the underlying substrate was added to the incoming flux on the top layer of FD mesh. The penetrating laser flux was calculated via Eq. 21 without the A_i term. All remaining laser irradiation is absorbed by the top layer of the FD mesh since the penetration depth through solid metals is typically $\mathcal{O}$ (nm). Thus the boundary condition for the top face can be expressed as $K\frac{\partial T}{\partial z}\Big|_{L_z} = q_{i,j}$ where $q_{i,j}$ is the portion of flux (from both conduction and the laser) hitting nodal point (i, j) on the top face of the substrate. The derivative term is approximated using the second order accurate, 3 point finite difference stencil of the form

$$\left.\frac{\partial T}{\partial z}\right|_{L_z} \approx \frac{1}{2\Delta z}((3T(x,y,L_z) - 4T(x,y,L_z-\Delta z) + T(x,y,L_z-2\Delta z)). \tag{27}$$

To account for phase changes within the substrate, we employ the same method of computationally raising the specific heat of the material in a small range around the melting temperature for those nodes which reach a temperature of at least $T_m - \frac{\Delta T}{2}$ (see Eq. 24). However, in this instance the density is also updated when the material changes phase. Note that the thermal conductivity is also expected to vary as the material changes phase; however, due to limited information as to the liquid thermal conductivity values for many materials, it is assumed to stay constant at the solid values in this simulation. Also note that heat capacity, thermal conductivity, and density are updated as a function of temperature within the solid phase.

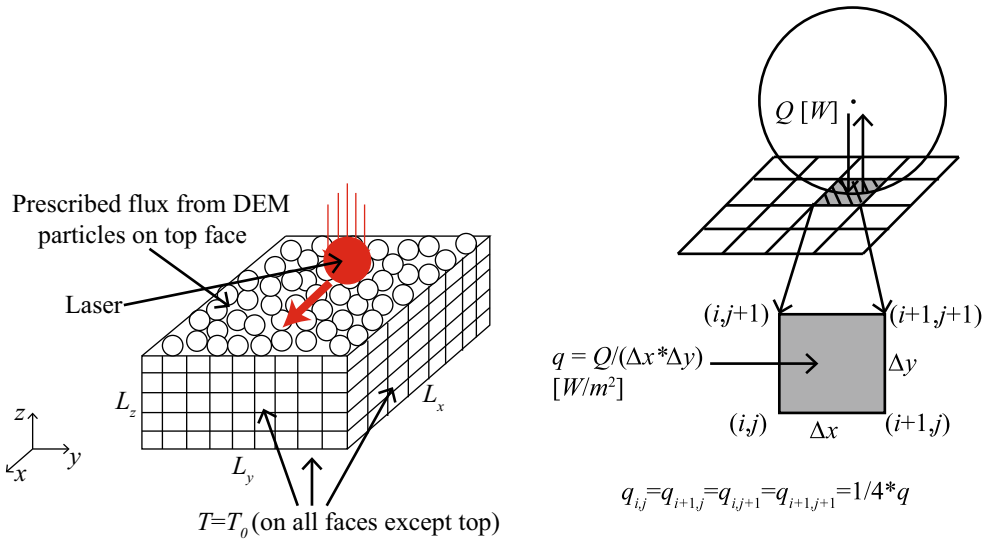

Fig. 6 Depiction of boundary conditions used for the finite difference mesh: all B.C.s (*left*), Neumann B.C. for top face (*right*). *Left figure* also depicts the path of the laser moving through the domain

3 Numerical solution scheme

To solve the coupled mechanical-thermal system, purely explicit time stepping schemes were utilized as they provided enough accuracy and efficiency for the current problem. Note that implicit schemes could easily be employed as well, with the advantage of increased stability regions allowing one to take larger time steps. However, implicit schemes require either iterations within each time step or large matrix inversions (for 3D FD schemes), which also increase computation time; thus creating a trade-off. Equation 1 was solved for the new position of each particle by decomposing this 2nd order differential equation into a series of first order equations. If we define $\mathbf{X}_i = \left\{ \begin{array}{c} \mathbf{v}_i \\ \mathbf{x}_i \end{array} \right\}$, then we can recast Eq. 1 as

$$\dot{\mathbf{X}}_i = \left\{ \begin{array}{c} \frac{1}{m_i}\mathbf{F}_i^{total} \\ \mathbf{v}_i \end{array} \right\} = f(\mathbf{X}_i, t), \tag{28}$$

where $\mathbf{v}_i$ and $\mathbf{x}_i$ represent the velocity and position of the i-th particle, respectively. This first order, vector system of equations, was marched forward in time using a fourth order explicit Runge–Kutta scheme [23] as follows

$$\begin{aligned}
\mathbf{Y}_1 &= \mathbf{X}_i(t), \\
\mathbf{Y}_2 &= \mathbf{X}_i(t) + \frac{1}{2}\Delta t f\left(\mathbf{Y}_1, t\right), \\
\mathbf{Y}_3 &= \mathbf{X}_i(t) + \frac{1}{2}\Delta t f\left(\mathbf{Y}_2, t + \frac{\Delta t}{2}\right), \\
\mathbf{Y}_4 &= \mathbf{X}_i(t) + \Delta t f\left(\mathbf{Y}_3, t + \frac{\Delta t}{2}\right), \\
\mathbf{X}_i(t+\Delta t) &= \mathbf{X}_i(t) + \frac{\Delta t}{6}\left[f(\mathbf{Y}_1, t) + 2f\left(\mathbf{Y}_2, t + \frac{\Delta t}{2}\right)\right. \\
&\quad \left. + 2f\left(\mathbf{Y}_3, t + \frac{\Delta t}{2}\right) + f(\mathbf{Y}_4, t + \Delta t)\right].
\end{aligned} \tag{29}$$

During the deposition process, only the mechanical equations required solving as the temperatures of each particle were considered fixed. Temperature rise due to collisions and small deformations was assumed to be negligible and thus not considered (indeed during the sintering/melting phase, energy input from the laser dominates all other heat transfer mechanisms). After deposition of a layer of particles, their positions were assumed to be fixed as a laser passed over the domain. At this time the thermal equations (Eqs. 18 and 25) were solved for each particle and FD node. A standard Forward Euler time-marching scheme was used for both the particles and FD nodes where $T_i(t+\Delta t) \approx T_i(t) + \Delta t \cdot \dot{T}_i(t)$ for each particle and $T(x, y, z, t+\Delta t) \approx T(x, y, z, t) + \Delta t \cdot \dot{T}(x, y, z, t)$ for each nodal point.

To decrease computation time, a binning algorithm is used whereby the particle domain is decomposed into grid sections, or bins, as illustrated in Fig. 7. Thus only particles within the same or neighboring bins are checked against each other to see if there is any contact. With correct implementation, such an algorithm can reduce the number of operations per time step from $\mathcal{O}(N^2)$ to $\mathcal{O}(N)$, resulting in a dramatic decrease in run time. More details regarding the implementation of such an algorithm and other variations can be found in [30]. The overall solution algorithm is summarized in Fig. 8.

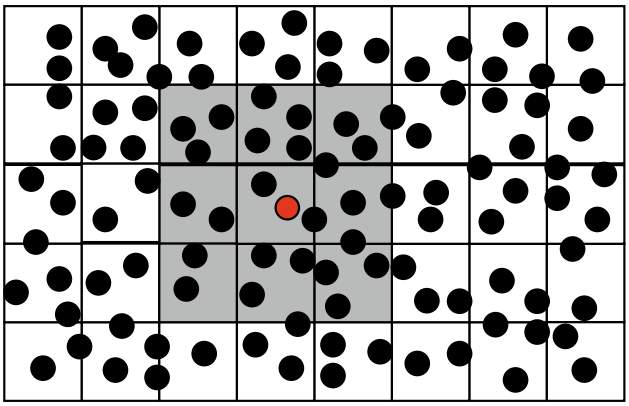

Fig. 7 Illustration of binning algorithm. Only particles in the shaded boxes will be checked for contact with the *red particle* in the center box (color figure online)

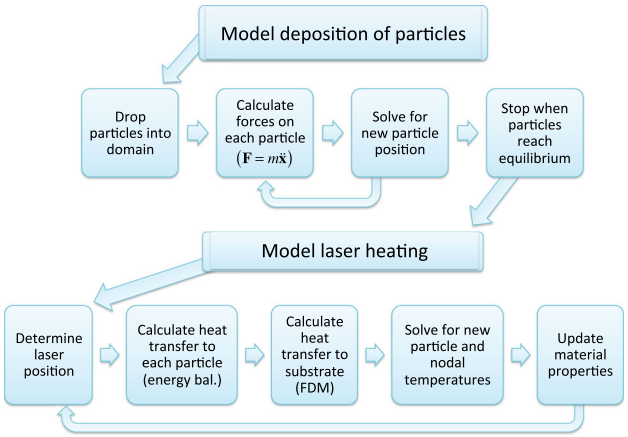

Fig. 8 Simulation flow chart

Finally, it should be noted that the FD formulation presented is second order accurate in space and first order accurate in time. However, due to the well-known stability conditions for such explicit schemes [23], the time step is proportional to the square of the grid spacing, or $\Delta t \propto (\Delta x)^2$. Thus the time step must be divided by four every time the grid increment is halved. Since there are three spatial dimensions, if the grid increment in each direction is halved, this equates to a 32-fold increase in computation time. Thus, clearly an optimal trade-off exists between using small enough grid increments to accurately capture the physics of the problem, while simultaneously not requiring an inordinate amount

Table 1 Material properties for 316L stainless steel as a function of temperature and phase [1]

Temperature (K)	Specific heat (J/kg K)	Thermal conductivity (W/m K)	Density (kg/m^3)
293	452	13.3	7952
366	485	14.3	7919
478	527	15.9	7877
589	548	17.5	7831
700	565	19.0	7786
811	573	19.8	7739
922	586	21.9	7692
1033	615	23.2	7640
1144	649	24.6	7587
1255	690	26.2	7537
1700 (liquid)	815	32.4	7300

of computation time. The convergence of this scheme was checked by calculating the same problem with grid increments continuously halved until no significant difference in results were obtained.

4 Validation

To validate this model, numerical simulations were carried out to recreate experiments conducted by Khairallah and Anderson [17]. Namely, the melt pool size predicted via this model was compared against the actual melt pool size during a single pass of a Gaussian laser over a single layer of powder particles sitting on a substrate.

This simulation was carried out using powder particles and a substrate of 316L stainless steel (316L SS). A Gaussian particle distribution was used with average diameter of 27 μm and a half-max-width of 10 μm. The particle coordinates were randomly generated at a height of 0.2–0.3 mm. The particles were dropped into a 1 mm × 0.5 mm cross-sectional domain domain and were allowed to settle for 0.1 s, after which they had essentially stopped moving. 600 total particles are used in this simulation, yielding a layer height of approximately 30 μm as specified in [17]. The particle packing density is calculated to be 45 %,[1] indicating a porosity of 55%. This is in close agreement with the reported density of approximately 42 % in [17]. These particles sit on top of a substrate with dimensions of $L_x = 1$ mm × $L_y = 0.5$ mm in cross-section and a depth of $L_z = 0.3$ mm. After the particles settled on the substrate, a laser was scanned over the domain in a single pass along the x-direction, as depicted in Fig. 6. The laser starts with its center point one spot size away from the domain and the simulation ends once the laser's center has moved one spot size past the other end of the domain. The laser beam is assumed to always hit the powder bed from a normal direction, or orthogonal to the plane of the powder bed. To avoid BC effects, the laser is centered on the plane $y = \frac{L_y}{2} = 0.25$ mm and the melt pool size is taken in the middle of the domain at the plain $x = \frac{L_x}{2} = 0.5$ mm. Larger simulations were modeled as well and the melt pool size did not change, indicating that this technique and domain size are appropriate in mitigating BC effects.

There are 201 × 101 × 61 grid nodes for the finite difference mesh yielding a grid spacing of $\Delta x = \Delta y = \Delta z = 5$ μm. The specific heat, thermal conductivity, and density values of 316L SS as a function of temperature are given in Table 1 [1]. Note that these values are linearly interpolated at temperature values in between the specified points. The data is extrapolated up to 1400 K (the final measured values are at 1255 K), after which the property values are fixed until phase change at 1700 K. Other material properties and simulation parameters used are provided in Table 2. A time step size of $\Delta t = 2 \times 10^{-8}$ s is used when solving the mechanical equations during the deposition process and a time step of

Table 2 Remaining material properties and simulation parameters used [1]

Parameter	Symbol	Value
Young's modulus	E	193 GPa
Poisson's ratio	ν	0.26
Damping parameter	ζ	0.1
Dynamic friction coefficient	μ_d	0.1
Viscosity of argon gas	μ_f	2.1×10^{-5} Pa s
Heat transfer coefficient	h	40 W/m^2 K
Melting temperature	T_m	1700 K
Boiling temperature	T_v	3130 K
Latent heat of melting	L_m	2.99×10^5 J/kg
Latent heat of vaporization	L_v	6.09×10^6 J/kg
Material emissivity	ϵ	0.33
Material absorptivity	α	0.33
Powder bed porosity	γ	0.55
Laser power	$Power$	200 W
Laser scan speed	v_{laser}	2.0 m/s
Laser spot size	w	54 μm
Preheat temperature	T_0	363 K
Environment temperature	T_{env}	363 K

[1] The powder bed density is calculated by adding the volume of all portions of all particles located within a 30 μm layer from the bottom substrate and then dividing by the volume of this layer (the cross section of the layer is 1000 μm × 500 μm and height is 30 μm).

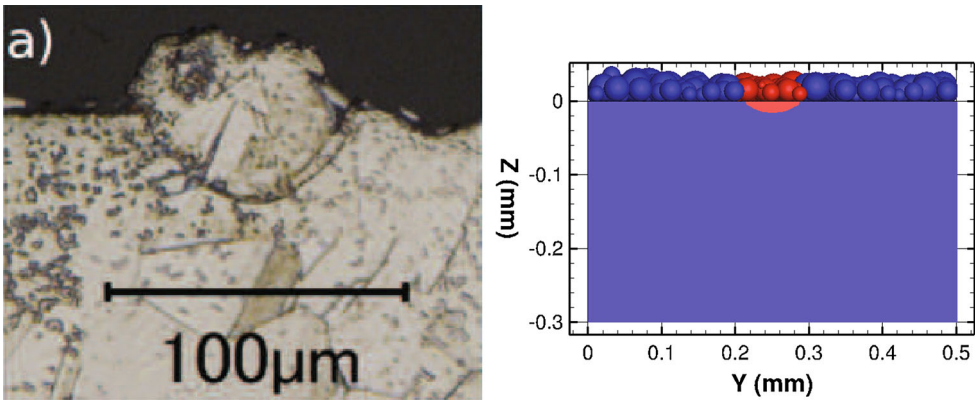

Fig. 9 Comparison of experimental melt pool size by Khairallah and Anderson (*left*) [17] and simulation melt pool size depicted in *red* (*right*). Note that the figure on the *left* is Fig. 5a from [17]. The experimental melt height, width, and depth are 26, 75, and 30 μm, respectively. The simulation melt pool dimensions are 30, 85, and 20 μm (color figure online)

$\Delta t = 5 \times 10^{-9}$ s is used when solving the thermal problem as the laser is scanned over the powder bed. These time steps were chosen such that the simulation remained stable and the results did not change when the time step was further reduced. Similarly, the grid spacing for the FD mesh was chosen such that the results did not significantly change when further refined.

Figure 9 shows a depiction of the simulation melt pool size vs. the actual melt pool size in the experiments by Khairallah and Anderson [17]. The experimental melt height, width, and depth are 26, 75, and 30 μm, respectively. The simulation melt pool dimensions are 30, 85, and 20 μm. These results show pretty good agreement with the experiments and are also close to the simulations carried out by Khairallah and Anderson [17] of this same experiment where they predicted a melt pool height, width, and depth of 26, 72, and 20 μm. The main source of error is believed to lie in the fact that the current simulation does not take into account consolidation mechanisms upon melting. Namely, one would expect the melt pool to be slightly lower in height than the original powder layer as the melted liquid coalesces and densifies, which would explain why the experimental melt height is less than the initial powder layer height of 30 μm (a feature which cannot be captured by this model). Additionally, Marangoni convection due to surface tension differences in hot and cold regions would serve to transfer more heat to the substrate and could explain the increased depth of the experimental melt pool. If the surface tension increases with temperature, and is higher in the center of the melt pool, this causes flow of material from outer regions of low surface tension towards the center where there is increased surface tension. This will cause the formation of a narrow and deep melt pool, which could be a significant factor in the increased depth and decreased width of the experimental melt pool as compared to the simulation. Limmaneevichitr and Kou [24] showed the propensity for Marangoni convection to form such a melt pool in steels under certain conditions, especially as beam spot size decreased. Additional sources of error could include the changing absorptivity of the material as it heats up and then melts (typically liquid metals are more reflective) and the analytical estimate used when determining the laser penetration into the powder bed.

However, it should be mentioned that the experimental results compared for model validation has process parameters more associated with SLM than SLS. As such, significant melting and consolidation occurs in the experimental results, which are not captured by this model. There are 2 main reasons that this model for SLS is compared against an experiment from the SLM literature: (1) a common technique for model validation in this field is comparing predicted and experimental melt pool size due to difficulties associated with exact measurements of the powder bed temperature, and (2) lack of thoroughly documented experimental results for strictly SLS which the authors could compare their model against. Despite this, the current simulation results are still qualitatively similar to the experimental results in [17]. Additionally, the coupled DE–FD simulation framework described in this work and implemented by the authors only required about 3 CPU hours to run on a MacBook Pro laptop computer. In comparison, the ALE framework used in the simulations from [17], required on the order of 100,000 CPU hours. Thus, this model shows promise as a quick tool to predict melt size, which can be extremely useful when determining optimal process parameters (i.e. hatch spacing, layer thickness, laser power, scan speed, powder size, etc.) during SLS. Recall only partial melting of metals occurs during typical SLS processes so the importance of consolidation mechanisms is reduced.

There are a couple of additional remarks the authors would like to make here. First, since consolidation mechanisms after melting are not accounted for in this model, the melt height provided by the simulation will always be equal to the initial layer height, 30 μm here, so long as complete melting of the particles occurs. As the combined melt height and depth predicted by this model is 50 μm, which is close to the experimental value of 56 μm, this model certainly shows promise as a quick guide for determining optimal process parameters. Second, a sensitivity study was performed to investigate the effect of changing the heat transfer coefficient and emissivity of the particles. However, no appreciable change in the

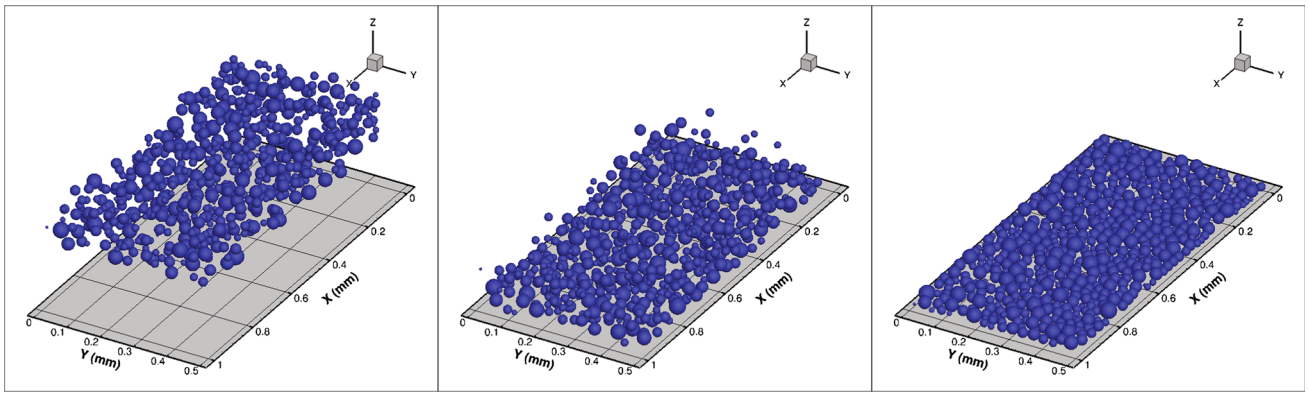

Fig. 10 Screenshots depicting the deposition of a layer of 316L SS particles (600 particles total)

results was noticed (during the time frame simulated) as these parameters were varied. A quick order-of-magnitude analysis explains this fact by showing that laser irradiation is by far the dominant heat transfer mechanism during the heating phase.

$$\begin{aligned}
\frac{q_{cond}}{q_{laser}} &\approx \frac{K(T_i - T_0)/D_i}{\alpha I_0} \approx \mathcal{O}(10^{-1}) \\
\frac{q_{conv}}{q_{laser}} &\approx \frac{h_{conv}(T_i - T_{env})}{\alpha I_0} \approx \mathcal{O}(10^{-5}) \\
\frac{q_{rad}}{q_{laser}} &\approx \frac{\epsilon \sigma_{SB}(T_i^4 - T_{env}^4)}{\alpha I_0} \approx \mathcal{O}(10^{-4})
\end{aligned} \tag{30}$$

These values were calculated by using the simulation parameters listed in Tables 1 and 2. The temperature values used were $T_0 = T_{env} = 363\,\text{K}$ and $T_i = 3130\,\text{K}$, the maximum temperature in the simulation (no particles had fully evaporated) representing the highest possible amount of heat transfer through conduction, convection, and radiation. The length scale for conduction from particle to substrate was $D_i = 27\ \mu\text{m}$, the average particle diameter. Also note that these are heat flux values and not total heat transfer. In the case of conduction, the contact area for solid particles is extremely small, which would make the ratio of total heat transfer, Q_{cond}/Q_{laser}, much lower for the powder particles (though this contact area will increase as the particles begin to melt). For cooling considerations, the influence of the other heat transfer mechanisms becomes much more apparent, with conduction being dominant.

5 Numerical examples

The intent of this section is to more fully illustrate the outputs and capabilities of the presented SLS model. First, a more detailed look at the results of the validation simulation described in the previous section are presented. Next, different parameter studies were performed by varying the laser power, scan speed, and powder size distribution.

Figure 10 shows screenshots depicting the deposition of the 316L SS particles from the validation simulation. It is worth mentioning here that the damping parameter value of $\zeta = 0.1$ was chosen such that the capabilities of the model in simulating particle-to-particle and particle-to-wall interactions are clearly visible. Simulations run using higher ζ values (up to 0.4), as may be more realistic of powder particles, allowed the particles to settle more quickly but did not significantly affect the geometry of the powder layer. Thus the given ζ value was used solely for illustration purposes. After the particles had settled, Fig. 11 shows screenshots of the temperature evolution of the particles and underlying substrate during the laser pass. All parameters in these two figures are identical to the ones provided in Tables 1 and 2.

In Fig. 11 notice how part of the underneath substrate gets melted as the laser passes over (recall 1700 K is the melting temperature). This is desirable to ensure proper bonding between layers during the SLS/SLM process. Note that in this simulation, the FD mesh represents the underneath substrate; however, this method could also be used to simulate previously solidified underneath layers. Figure 12 depicts how the melt pool size (depth and width) changes as the laser power and scan speed are varied, respectively. It is again worth mentioning that the laser is centered on the plane $y = \frac{L_y}{2} = 0.25\,\text{mm}$ and the melt pool size is taken in the middle of the domain at the plain $x = \frac{L_x}{2} = 0.5\,\text{mm}$ to avoid BC effects. The melt depth plotted refers to the depth that the underlying substrate layer gets melted. It is necessary for some melting (or re-melting) of the underneath layer to occur for proper bonding between layers (indicated by the melt depth). The melt pool width can give a good indication of the optimal hatch spacing, or distance between laser passes. Again, some melt pool overlap between adjacent laser passes is necessary for proper bonding and a smoother surface finish [32]. With such information, the laser power and scan speed can

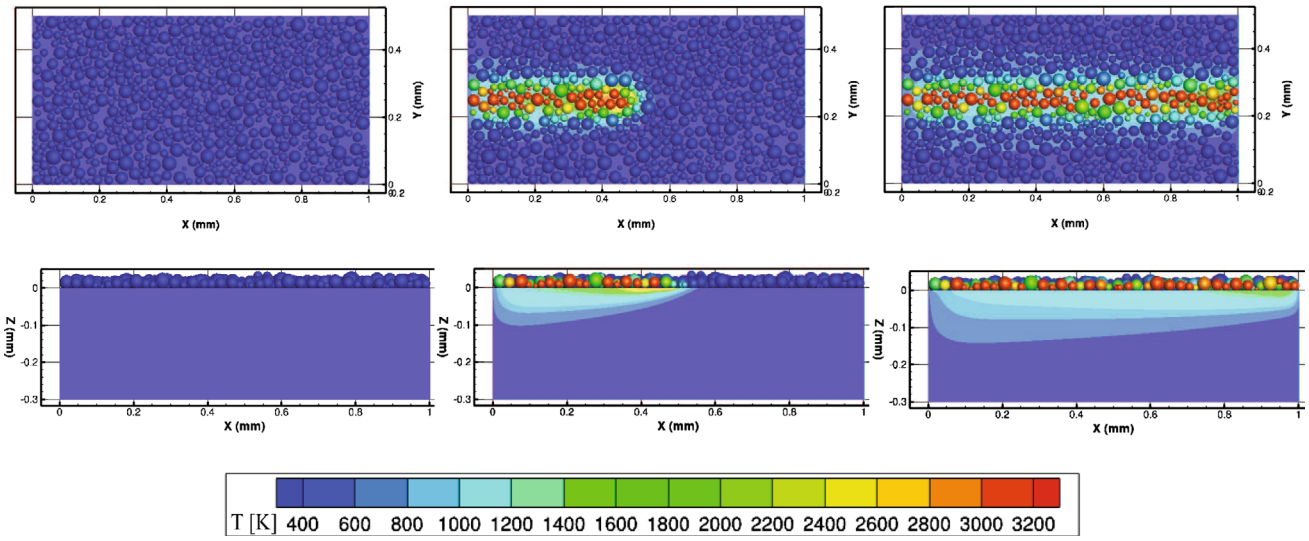

Fig. 11 Screenshots showing the temperature evolution of a layer of 316L SS particles and the underlying 316L SS substrate as a laser is passed over (temperature in Kelvin). *Top view* on *upper row*. *Cross-sectional view* from the side on *bottom row* (color figure online)

be optimized to reduce total processing time and use as little energy input as possible, while still producing usable parts.

An additional advantage of this model over conventional continuum type models is the ability to capture inhomogeneities in the powder bed layer and the ability to simulate different powder size distributions. Table 3 shows how different powder size distributions can affect the density of the loose powder bed. Recall Korner et al. [19,20] found that the loose powder bed density had the greatest effect on final part density during simulations and experiments run on selective electron beam melting. From Table 3 it can be seen how the loose bed density increases as the spread of the powder size distribution increases. This makes intuitive sense as one would expect smaller particles to fill in the voids between larger particles. Additionally, the last row of Table 3 shows the density of a bimodal powder distribution. In this distribution, smaller particles (with mean diameter of 8 μm) are mixed with larger particles (with a mean diameter of 30 μm). This bimodal distribution represents the largest loose bed density, as should be expected.

While this bimodal distribution clearly increases the loose bed density, one would expect a bimodal distribution with even smaller particles to only further increase this loose bed density and hence yield higher final part densities. However, as the smaller particles get interspersed with larger particles, these smaller particles may start to vaporize before the larger particles melt when a laser is scanned over the bed. These vaporized particles may get trapped as gas bubbles in the final part which will decrease the final density and strength [22]. Thus an optimal size distribution must exist to maximize loose bed density while minimizing the vaporization of smaller particles. Indeed in Fig. 13, this exact situation is simulated for a 30 μm layer of 316L SS particles. The laser

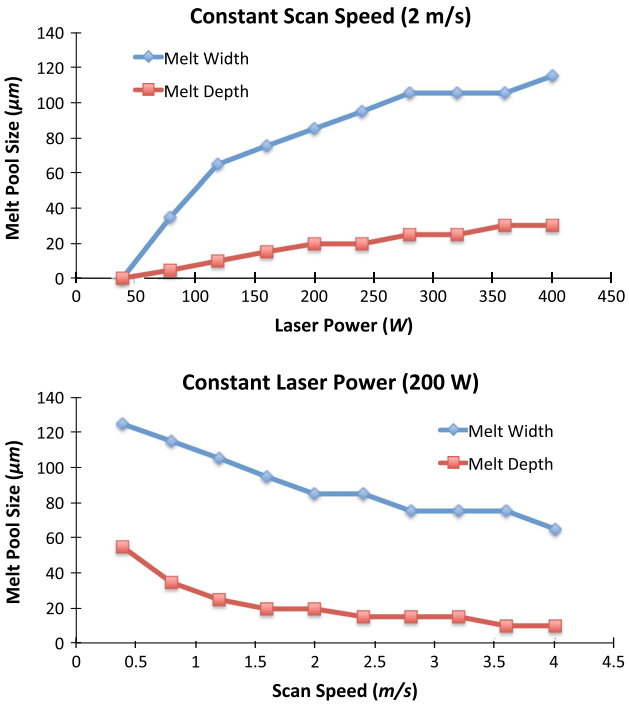

Fig. 12 Melt pool size as laser power is varied from 40 to 400 W with scan speed constant at 2.0 m/s (*top*), and melt pool size as scan speed is varied from 0.4 to 4.0 m/s with laser power constant at 200 W (*bottom*)

power is 200 W and scan speed is 2.0 m/s. The porosity (γ) for the laser penetration model is updated depending on the density of the powder layer, where porosity $= 1 - density$.

In the left image of this figure, a normal distribution of particles with mean diameter of 30 μm and standard deviation of 5 μm is used. The diameters of these particles were constrained to be between 20 and 40 μm. 550 of these parti-

Table 3 Affect of powder size distribution on loose bed density, last row represents a bimodal distribution

No. particles	Mean diameter (μm)	SD (μm)	Min (μm)	Max (μm)	Powder density (%)
550	30	1	10	50	46.4
550	30	3	10	50	48.6
550	30	5	10	50	51.4
550	30	7	10	50	52.4
550	30	10	10	50	54.0
550, 3000	30, 8	5, 2	20, 4	40, 12	55.5

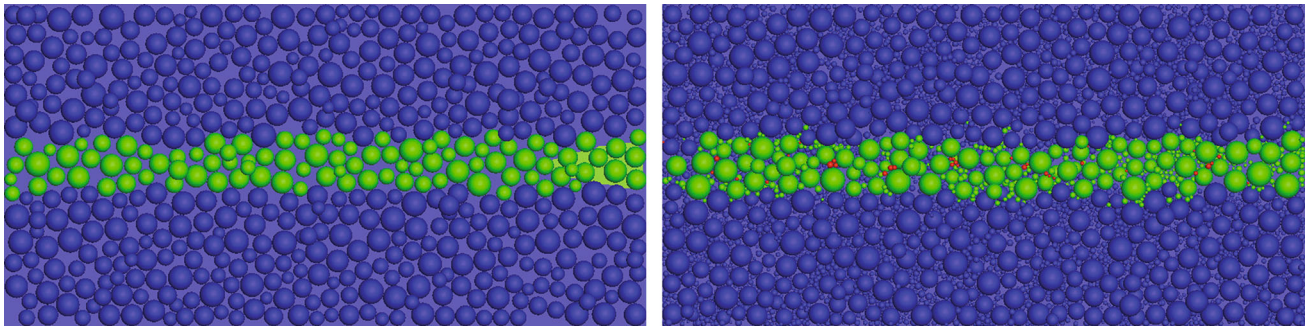

Fig. 13 Melt pool from a single laser pass over a mono-modal (*left*) and bimodal (*right*) powder distribution. Note that solid particles are *blue*, molten ones are *green*, and gaseous ones are *red*. Notice how some small particles are vaporized in the bimodal distribution. Laser power is 200 W and scan speed is 2.0 m/s. All parameters between the two simulations are identical other than particle size distribution (color figure online)

cles are deposited in a layer and a single pass of the laser is scanned over it. The phase of the particles are represented by color where blue represents solid, green represents liquid, and red represents vaporized particles. Notice how none of the particles are vaporized in the scenario where a mono-modal particle size distribution is used (left image), as desired. Now look at the right image of Fig. 13, which represents a bimodal distribution of particles. This distribution is the same as that indicated in the final row of Table 3. Notice here how some of the very small particles are red in color, indicating they have vaporized. Due to the rapid cooling and solidification rates present in the SLS/SLM process, these vaporized particles may be trapped as gas bubbles in the solidified part and decrease the final density. Alternatively, these ablated particles could increase the surface roughness of that layer and cause inhomogeneities in layer thickness if this issue persists over multiple layers. Obviously, one could prevent ablation of the small particles by decreasing the laser energy density (i.e. decrease power or increase scan speed); however, a decrease in input energy would prevent the underlying layer from being re-melted which would inhibit proper bonding between successive layers.

6 Conclusion

The overall goal of this research was to create a reduced order model of the SLS process that can be used to quickly guide process parameters (laser power, scan speed, hatch spacing, powder size, layer thickness, etc.) for different materials. This was achieved by considering a small representative domain and simulating the deposition and heating of powder particles and the underneath substrate as a laser passes over. A novel, coupled discrete element-finite difference framework was presented to simulate heat transfer from the powder particles to the underlying substrate during laser processing. The particles were modeled as thermally and mechanically interacting discrete elements, capturing inhomogeneities in the powder layer and avoiding the need to assign effective properties (i.e. thermal conductivity, heat capacity, density, etc.) as would be necessary in a traditional continuum model. Heat transfer through the solid, underlying substrate was modeled via the finite difference method. Note that this sort of technique could also be used to model previously solidified and now fully dense underneath layers. Validation was obtained through comparing the simulated melt pool size against experimental results in the literature, showing qualitative agreement.

By only simulating a small domain, writing the program in a high performance language (Fortran 90 in the present case), and using a binning algorithm, this reduced order model could be run in a matter of minutes to hours on a laptop computer. Further parallelization on multiple cores would further decrease necessary computation time. Clearly this fast simulation time is ideal for running many different iterations with different inputs to find an optimal window of process parameters or for performing sensitivity studies. Additionally, this framework easily enables the simulation of

a mixture of powder materials and sizes, such as one material with a high melting temperature surrounded by binder powder material of a lower melting temperature (a common practice in industry).

While this reduced order model was able to simulate a single laser pass in a reasonable amount of time, such a technique would not be computationally tractable for whole part-level simulations. In such a case, larger continuum models, such as FEM, would be necessary to simulate layer addition and residual stresses that build up in full size parts of arbitrary shapes. However, information from the DE modeling of the powder bed (such as powder bed thermal conductivity, loose powder bed density, melt pool size, etc.) can provide important inputs into larger-scale continuum models for a multi-scale approach to entire part size simulations.

Improvements can be made to this model by allowing for thermal expansion and shrinkage of the particles, gas-gap-conduction between particles, and especially fluid flow upon melting. Additionally, the effects of radiative pressure on the powder bed are worth investigating as this could aid in consolidation, especially when using high frequency pulsed lasers [8,9]. In regards to fluid flow and consolidation of the powder bed, the authors are currently investigating a few methods within the existing framework. Potential techniques include: (1) assigning molten particles a significantly reduced stiffness to simulate the "softer" fluid, (2) breaking molten particles into many separate "fluid" particles governed by different constitutive laws, or (3) treating molten particles as a continuum and employing a hybrid discrete element-continuum simulation approach. Option 1 is more of an ad-hoc approach but may offer more accuracy in representing the increased heat transfer that would occur upon melting (since a lower particle stiffness would increase the contact area for conduction to occur). Options 2 and 3 could offer more qualitatively realistic simulations but would significantly increase the computational expense. It is worth noting here that the feasibility of coupling DE particles with a continuum model for fluid flow has been previously demonstrated [10,37], but not for the case of melting which would require the immediate switch from a DE particle to a continuum method. It is also worth noting that consolidation of the melt pool typically takes place during a time frame of $\mathcal{O}$ (ms) to $\mathcal{O}$(10 ms) [15], which is significantly longer than the time frame of these simulations (at a scan speed of 2.0 m/s, the domain is only under laser irradiation for slightly over 0.5 ms). Simulating for a much longer time frame to accurately account for all consolidation mechanisms and allow for re-solidification of the melt pool is beyond the scope of the current framework, which is meant for rapid computations and quick estimations of ideal process parameters. However, with increased computational power and parallelization across many cores, the options described above are certainly feasible.

As a closing comment the authors would like to mention the relative newness of the SLS/SLM process (indeed only in the past decade has this technology really taken off as a viable final product manufacturing technique). As such, there still remains lots of research on new ways to improve this process and to innovate in this field. Various companies are trying different techniques, such as the use of multiple lasers, extremely high powered lasers, novel optics, etc. to be able to 3D print complicated features and larger parts more efficiently. Other approaches include cold spraying particles onto the substrate to achieve plastic deformation and reduce the laser power needed for melting, or laser induced forward transfer (LIFT) where prefabricated structures are printed onto a substrate. Modifications to computational models such as this could be used to simulate these novel laser-based AM techniques and aid in the design of new machinery by evaluating the feasibility of such processes.

Acknowledgments The authors would like to express their gratitude towards Ramesh Subramanian and Marco Brunelli of Siemens Energy, Inc. for funding this research. Additionally, the input of other members of the Siemens Corporation was useful in the formulation and validation of this approach. Finally the authors would like to thank fellow members of the CMRL lab at UC Berkeley for many fruitful discussions and their aid in the proofreading and editing of this paper.

References

1. Mechanical and physical properties of the austenitic chromium–nickel stainless steels at elevated temperatures 3rd edn. The International Nickel Company Inc., New York (1968)
2. Adams, G., Nosonovsky, M.: Contact modeling—forces. Tribol. Int. **33**, 431–442 (2000)
3. Antony, K., Arivazhagan, N., Senthilkumaran, K.: Numerical and experimental investigations on laser melting of stainless steel 316L metal powders. J. Manuf. Process. **16**(3), 345–355 (2014)
4. Bonacina, C., Comini, G., Fasano, A., Primicerio, M.: Numerical solution of phase-change problems. Int. J. Heat Mass Transf. **16**(10), 1825–1832 (1973)
5. Campello, E.M., Zohdi, T.I.: A computational framework for simulation of the delivery of substances into cells. Int. J. Numer. Methods Biomed. Eng. **30**, 1132–1152 (2014)
6. Dai, D., Gu, D.: Thermal behavior and densification mechanism during selective laser melting of copper matrix composites: Simulation and experiments. Mater. Des. **55**, 482–491 (2014)
7. Dong, L., Makradi, A., Ahzi, S., Remond, Y.: Three-dimensional transient finite element analysis of the selective laser sintering process. J. Mater. Process. Technol. **209**(2), 700–706 (2009)
8. Ebert, R., Ullmann, F., Hildebrandt, D., Schille, J., Hartwig, L., Kloetzer, S., Streek, A., Exner, H.: Laser processing of tungsten powder with femtosecond laser radiation. J. Laser Micro Nanoeng. **7**(1), 38–43 (2012)
9. Fischer, P., Locher, M., Romano, V., Weber, H., Kolossov, S., Glardon, R.: Temperature measurements during selective laser sintering of titanium powder. Int. J. Mach. Tools Manuf. **44**(12–13), 1293–1296 (2004)
10. Galindo-Torres, S.: A coupled discrete element lattice Boltzmann method for the simulation of fluid solid interaction with particles of

general shapes. Comput. Methods Appl. Mech. Eng. **265**, 107–119 (2013)
11. Ganeriwala, R., Zohdi, T.I.: Multiphysics modeling and simulation of selective laser sintering manufacturing processes. Proc. CIRP **14**(0), 299–304 (2014). (6th CIRP international conference on high performance cutting, HPC2014)
12. Gusarov, A., Kruth, J.P.: Modelling of radiation transfer in metallic powders at laser treatment. Int. J. Heat Mass Transf. **48**(16), 3423–3434 (2005)
13. Gusarov, A.V., Yadroitsev, I., Bertrand, P., Smurov, I.: Model of radiation and heat transfer in laser-powder interaction zone at selective laser melting. J. Heat Transf. **131**(7), 072,101 (2009)
14. Hecht, J.: Understanding Lasers. Wiley, Hoboken (2008)
15. Hodge, N., Ferencz, R., Solberg, J.: Implementation of a thermomechanical model for the simulation of selective laser melting. Comput. Mech. **54**, 33–51 (2014)
16. Johnson, K.: Contact Mechanics. Cambridge University Press, Cambridge (1987)
17. Khairallah, S.A., Anderson, A.: Mesoscopic simulation model of selective laser melting of stainless steel powder. J. Mater. Process. Technol. **214**(11), 2627–2636 (2014)
18. Kolossov, S., Boillat, E., Glardon, R., Fischer, P., Locher, M.: 3D FE simulation for temperature evolution in the selective laser sintering process. Int. J. Mach. Tools Manuf. **44**(2–3), 117–123 (2004)
19. Körner, C., Attar, E., Heinl, P.: Mesoscopic simulation of selective beam melting processes. J. Mater. Process. Technol. **211**(6), 978–987 (2011)
20. Körner, C., Bauereiß, A., Attar, E.: Fundamental consolidation mechanisms during selective beam melting of powders. Modell. Simul. Mater. Sci. Eng. **21**(8), 085,011 (2013)
21. Kruth, J.P., Levy, G., Klocke, F., Childs, T.: Consolidation phenomena in laser and powder-bed based layered manufacturing. CIRP Ann. Manuf. Technol. **56**(2), 730–759 (2007)
22. Kumar, S.: Comprehensive Materials Processing, vol. 10. Elsevier, Amsterdam (2014)
23. LeVeque, R.: Finite Difference Methods for Ordinary and Partial Differential Equations: Steady-State and Time-Dependent Problems. Society for Industrial and Applied Mathematics, Philadelphia (2007)
24. Limmaneevichitr, C., Kou, S.: Experiments to simulate effect of Marangoni convection on weld pool shape. Weld. J. **79**, 231s–237s (2000)
25. Maeda, K., Childs, T.: Laser sintering (SLS) of hard metal powders for abrasion resistant coatings. J. Mater. Process. Technol. **149**(1–3), 609–615 (2004)
26. Matsumoto, M., Shiomi, M., Osakada, K., Abe, F.: Finite element analysis of single layer forming on metallic powder bed in rapid prototyping by selective laser processing. Int. J. Mach. Tools Manuf. **42**(1), 61–67 (2002)
27. Muhieddine, M., Canot, E., March, R.: Various approaches for solving problems in heat conduction with phase change. Int. J. Finite Vol. **6**, 66–85 (2009)
28. Munson, B., Young, D., Okiishi, T.: Fundamentals of Fluid Mechanics. Wiley, Hoboken (2005)
29. Nelson, J., Xue, S., Barlow, J.W., Beaman, J.J., Beaman, J., Marcus, H.L., Bourell, D.: Model of the selective laser sintering of bisphenol-A polycarbonate. Ind. Eng. Chem. Res. **32**, 2305–2317 (1993)
30. Perkins, E.D., Williams, J.R.: Generalized spatial binning of bodies of different sizes. In: Cook, B.K., Jensen, R.P. (eds.) Discrete Element Methods: Numerical Modeling of Discontinua, pp. 52–55. ASCE, Reston (2002)
31. Schmidt, M., Pohle, D., Rechtenwald, T.: Selective laser sintering of PEEK. CIRP Ann. Manuf. Technol. **56**(1), 205–208 (2007)
32. Shifeng, W., Shuai, L., Qingsong, W., Yan, C., Sheng, Z., Yusheng, S.: Effect of molten pool boundaries on the mechanical properties of selective laser melting parts. J. Mater. Process. Technol. **214**, 2660–2667 (2014)
33. Simchi, A.: Direct laser sintering of metal powders: mechanism, kinetics and microstructural features. Mater. Sci. Eng. A **428**(1–2), 148–158 (2006)
34. Simchi, A., Pohl, H.: Effects of laser sintering processing parameters on the microstructure and densification of iron powder. Mater. Sci. Eng. A **359**(1–2), 119–128 (2003)
35. Steen, W.M., Mazumder, J.: Laser Material Processing. Springer, London (2010)
36. Tan, K., Chua, C., Leong, K., Cheah, C., Cheang, P., Abu Bakar, M., Cha, S.: Scaffold development using selective laser sintering of polyetheretherketone hydroxyapatite biocomposite blends. Biomaterials **24**(18), 3115–3123 (2003)
37. Wellmann, C., Wriggers, P.: A two-scale model of granular materials. Comput. Methods Appl. Mech. Eng. **205–208**, 46–58 (2012)
38. Williams, J.M., Adewunmi, A., Schek, R.M., Flanagan, C.L., Krebsbach, P.H., Feinberg, S.E., Hollister, S.J., Das, S.: Bone tissue engineering using polycaprolactone scaffolds fabricated via selective laser sintering. Biomaterials **26**(23), 4817–27 (2005)
39. Zeng, K., Pal, D., Stucker, B.: A review of thermal analysis methods in laser sintering and selective laser melting. In: 23rd Annual International Solid Freeform Fabrication Symposium—An Additive Manufacturing Conference, pp. 796–814 (2012)
40. Zohdi, T.: Rapid simulation of laser processing of discrete particulate materials. Arch. Comput. Methods Eng. **20**(4), 309–325 (2013)
41. Zohdi, T.: Additive particle deposition and selective laser processing-a computational manufacturing framework. Comput. Mech. **54**, 171–191 (2014)
42. Zohdi, T.: A direct particle-based computational framework for electrically enhanced thermo-mechanical sintering of powdered materials. Math. Mech. Solids **19**(1), 93–113 (2014)